

# In Situ Pyrolysis of 3D Printed Building Blocks for Functional Nanoscale Metamaterials

Qing Sun, Christian Dolle, Chantal Kurpiers, Kristian Kraft, Monsur Islam, Ruth Schwaiger, Peter Gumbsch, and Yolita M. Eggeler\*

This study presents a novel approach for investigating the shrinkage dynamics of 3D-printed nanoarchitectures during isothermal pyrolysis, utilizing in situ electron microscopy. For the first time, the temporal evolution of 3D structures is tracked continuously until a quasi-stationary state is reached. By subjecting the 3D objects to different temperatures and atmospheric conditions, significant changes in the resulting kinetic parameters and morphological textures of the 3D objects are observed, particularly those possessing varying surface-to-volume ratios. Its results reveal that the effective activation energy required for pyrolysis-induced morphological shrinkage is approximately four times larger under vacuum conditions than in a nitrogen atmosphere (2.6 eV vs. 0.5–0.9 eV, respectively). Additionally, a subtle enrichment of oxygen on the surfaces of the structures for pyrolysis in nitrogen is found through a postmortem electron energy loss spectroscopy study, differentiating the vacuum pyrolysis. These findings are examined in the context of the underlying process parameters, and a mechanistic model is proposed. As a result, understanding and controlling pyrolysis in 3D structures of different geometrical dimensions not only enables precise modification of shrinkage and the creation of tensegrity structures, but also promotes pyrolytic carbon development with custom architectures and properties, especially in the field of carbon micro- and nano-electromechanical systems.

achievable.<sup>[1]</sup> 3D printing has even found its way into everyday life and commercially available tools allow the access to the fascinating world of printing all conceivable structures in a bottom up approach. In the scientific community, several distinguished approaches are used to bring the used precursor matter into 3D order.<sup>[2–6]</sup> One of the most promising techniques is the light stimulated polymerization of oligomeric organic precursor materials by two-photon direct laser writing (DLW).<sup>[6,7]</sup>

In DLW printed architectures, a polymer solution is spread on a surface and the subsequent cross-linking is stimulated by the application of focussed laser light, thus allowing the construction of 3D structures with structural sizes close to the diffraction limit of the employed light source.<sup>[6]</sup> The versatility of this printing technique was already used to conceive microstructural architectures to be employed in fields related to carbon microelectromechanical systems (C-MEMS), building devices that act as biosensors,<sup>[8]</sup> lab-on-a-chip,<sup>[9,10]</sup> drug delivery,<sup>[11,12]</sup> or tissue engineering.<sup>[13,14]</sup> To further miniaturize these printed microstructures, pyrolysis

in a vacuum or under an inert atmosphere is an established processing step, leading to a structural shrinkage of up to 80%<sup>[6,15]</sup> and the accompanied evolution of the resulting materials' parameters, such as electrical, optical, and mechanical

## 1. Introduction

With the advent of novel printing techniques, a vast majority of ultra-complex micro- and nanoarchitectures are nowadays easily

Q. Sun, C. Dolle, K. Kraft, Y. M. Eggeler  
Microscopy of Nanoscale Structures & Mechanisms (MNM)  
Laboratory for Electron Microscopy (LEM)  
Karlsruhe Institute of Technology (KIT)  
76131 Karlsruhe, Germany  
E-mail: yolita.eggeler@kit.edu

C. Kurpiers, P. Gumbsch  
Institute for Applied Materials (IAM)  
Karlsruhe Institute of Technology (KIT)  
76131 Karlsruhe, Germany

M. Islam  
Institute of Microstructure Technology (IMT)  
Karlsruhe Institute of Technology (KIT)  
76344 Eggenstein-Leopoldshafen, Germany

R. Schwaiger  
Institute of Energy and Climate Research (IEK)  
Forschungszentrum Jülich GmbH  
52428 Jülich, Germany

P. Gumbsch  
Fraunhofer Institute for Mechanics of Materials (IWM)  
79108 Freiburg, Germany

 The ORCID identification number(s) for the author(s) of this article can be found under <https://doi.org/10.1002/adfm.202302358>

© 2023 The Authors. Advanced Functional Materials published by Wiley-VCH GmbH. This is an open access article under the terms of the Creative Commons Attribution-NonCommercial License, which permits use, distribution and reproduction in any medium, provided the original work is properly cited and is not used for commercial purposes.

DOI: 10.1002/adfm.202302358

properties.<sup>[6,13,16–19]</sup> 3D printed and pyrolyzed structures were e.g., used for applications in life science or micromechanical engineering, showing the broad applicability of the combination of 3D printing and pyrolysis. The predominant size reduction upon pyrolysis is already happening at relatively low temperatures below 600 °C,<sup>[20,21]</sup> while pyrolytically converted materials are usually heated to 900 °C and above to generate glassy carbon or graphenoid materials from the printed organic precursor material.<sup>[22]</sup>

Here, we use in situ scanning electron microscopy (SEM) to investigate the size defining shrinkage step of 3D printed microstruts that are used as building blocks for mechanical metamaterials<sup>[6]</sup> to observe and quantify the structural alteration under real isothermal conditions and in different surrounding atmospheres. By unraveling the real-time structural shrinkage, we are able to use the tracked deformation dynamics to extract effective activation energies.<sup>[23]</sup> Furthermore, by employing the capabilities of environmental scanning electron microscopy (ESEM), we expand our study to two defined pressure states, namely high vacuum ( $10^{-5}$  mbar, HV) and low vacuum (3 mbar, LV) to address the differences in the two predominant pyrolysis regimes (in vacuum or inert atmosphere). The experiments are carried out using a micro-electromechanical-system (MEMS) chip heating system that allows high heating rates of  $20\text{ °C s}^{-1}$  to reach the final isothermal setpoints of 450, 500, and 550 °C. We track the longitudinal changes by SEM imaging and extract the effective activation energies by fitting a model-free master curve to the obtained data.<sup>[23]</sup> Finally, a postmortem scanning transmission electron microscopy (STEM) electron energy loss spectroscopy (EELS) investigation gives deeper insights into the distribution of carbon and oxygen. Our study is complemented by thermogravimetric analysis (TGA) measurements, showing not only the predominant weight loss at 500 °C but also helps to unravel the composition of the volatile byproducts that are released during the structural shrinkage.

The microstruts that we investigate in this study are the fundamental building blocks of complex architected metamaterial cages that show unprecedented mechanical properties under loading stress.<sup>[6,24–26]</sup> Their structural stability is hence directly correlated to the properties of its individual constituents after pyrolysis-induced shrinkage. To properly understand and predict these properties, a thorough understanding of the material response during the process of pyrolysis is therefore of utmost importance. We expect to get a glimpse of the pure pyrolysis mechanism based on our study to pave the way toward a complete understanding of parameters and processes for a better predictability of the resulting carbon materials' properties.

For this study, we used a commercially available photoresist, referred to as IP-Dip, which is an acrylate-based photoresist. It is known to comprise 60–80% of pentaerythritol triacrylate (also known as 2-(hydroxymethyl)-2-[[1-(1-oxoallyl)oxy]methyl]-1,3-propanediyl diacrylate), which is an oxygen-enriched monomer.<sup>[15,27]</sup> On the one hand, using TPL DLW and a well-known photoresist allows precise printing on the MEMS chip. On the other hand, there is research on IP-Dip derived carbon in different fields, from mechanical metamaterials,<sup>[6,24–26]</sup> and photonic structures<sup>[15]</sup> to C-MEMS applications.<sup>[27,28]</sup> Additionally, this in situ experimental pyrolysis design can be extended to investigations of various other polymer precursors.

## 2. Results and Discussion

### 2.1. Sample Design and Fabrication

Regarding the sample morphology, previous studies reported that different structures and especially the associated surface-to-volume ratios have a strong influence on the degree of shrinkage induced by pyrolysis.<sup>[29]</sup> However, structures fixed on a substrate will experience non-uniform shrinkage in the vertical direction due to the strong adhesion to the substrate.<sup>[29,30]</sup> We choose a series of microstrut structures with 10  $\mu\text{m}$  length and use springs and disc-shape pedestals as decoupling supports, as suggested in the literature.<sup>[6,31]</sup> Their cross sections were designed with varying squares with lateral dimensions of  $1 \times 1$ ,  $2 \times 2$ ,  $3 \times 3$ , and  $4 \times 4\ \mu\text{m}$  and are referred to in the following as G1, G2, G3, and G4, respectively. A cross-sectional analysis of the as-printed microstruts reveals an elongation in Z-direction, see Figure S1 (Supporting Information). The deviation of the perfect square shape can be explained by the intrinsic ellipsoidal voxels of the TPL system, where the vertical resolution is three times lower than the horizontal resolution.<sup>[15]</sup> Moreover, thicker samples tend to have some concave and convex shapes on their surfaces. This phenomenon may be assigned to the uneven degree of cross-linking caused by the overlapping of voxel lines in the printing process.

**Figure 1** depicts the schematic workflow for the in situ pyrolysis study. The protruding “ears” at both ends of the microstrut (as seen in Figure 1e) are used as tracking markers to better determine the actual (projected) lengths during shrinkage when exposed to heating. Thermogravimetric studies have shown that the mass loss and structural evolution mainly occurs in the initial temperature stage between 400–600 °C (see **Figure 2a**). It is caused by the formation of volatile byproducts, which degas out of the printed structures during pyrolysis. These volatile byproducts contain  $\text{CH}_4$ ,  $\text{H}_2\text{O}$ ,  $\text{CO}$ ,  $\text{HCOH}$ ,  $\text{CO}_2$ , etc. as evident by complementary mass-spectrometric measurements (see **Figure 2b**). Hence, we conduct isothermal heating experiments at 450, 500, and 550 °C to investigate the dynamics of the struts' structural evolution. Taking advantage of the rapid heating and precise temperature control of the heating chip,<sup>[33]</sup> the temperature set point is reached at a heating rate of  $20\text{ °C s}^{-1}$  (**Figure S2**, Supporting Information illustrates the temperature-time profiles). It is worth noting that pyrolysis studies are typically conducted under an inert gas atmosphere at ambient pressure. Among the used gases are nitrogen,<sup>[34,35]</sup> argon,<sup>[15]</sup> forming gas (5% hydrogen 95% nitrogen)<sup>[3]</sup> but also the behavior under high vacuum atmospheres was already investigated.<sup>[6,27]</sup> To correlate the effects of different atmospheric environments, we perform in situ ESEM experiments in two pressure regimes: under high vacuum (HV) of  $10^{-5}$  mbar and in a reduced nitrogen atmosphere of 3 mbar (LV) in order to extract the kinetic parameters as a function of different surface-to-volume ratios and propose a pyrolysis mechanism in relation to the atmospheric conditions.

### 2.2. In Situ ESEM Pyrolysis

In order to study the real-time pyrolysis behavior and mechanism of IP-Dip microstruts, we performed in situ heating ESEM experiments. To determine the evolution of the isothermal pyrolysis-induced shrinkage, we continuously recorded top-view images of

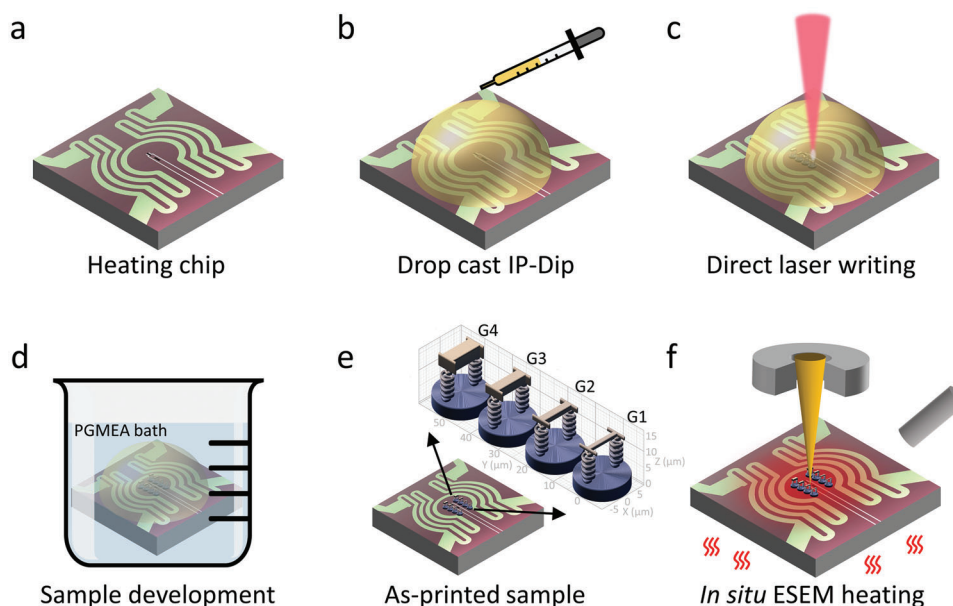


**Figure 1.** Schematic representation of the microstrut preparation steps onto the micro-electro-mechanical systems (MEMS) chip by two-photon DLW for in situ ESEM heating. a) MEMS heating chip with a centered heating zone of around 150  $\mu\text{m}$  diameter printable area is utilized for in situ heating experiments. b) IP-Dip photoresist is drop cast onto the heating zone. c) DLW enables 3D printing on any surface by moving ellipsoidal voxels in lateral and vertical directions. d) Any unpolymerized photoresist is removed by rinsing in developing solvent. e) As-printed microstruts with varying surface-to-volume ratios referred to as G1, G2, G3, and G4 are sitting in the heating zone center as indicated by the 3D rendering inset. f) In situ ESEM heating experiments are conducted by continuous image recording in different environments: high vacuum (HV) and low vacuum (LV) with nitrogen gas. Adapted with permission.<sup>[32]</sup> Copyright 2018, Springer Nature.

the microstruts by secondary electron imaging, as presented in **Figure 3**. Figure 3a–c represents a collection of SEM micrographs obtained at progressing times during isothermal exposures at 450, 500, and 550  $^{\circ}\text{C}$ , respectively, in high vacuum (HV) of  $10^{-5}$  mbar (The full datasets are presented as Movie S1–S3, Supporting Information). The same isothermal in situ pyrolysis experiment was also performed an inert atmosphere with increased

partial pressure (LV) by introducing nitrogen gas into the ESEM chamber, referred to as “low vacuum” (LV) experiments. To avoid redundancy, only the series of micrographs for the HV experiments are presented here, while the LV data are presented in the Figure S3 and Movie S4–S6 (Supporting Information). As mentioned above, for both isothermal in situ experiments, 3D-printed microstruts connected to springs on a pedestal were directly

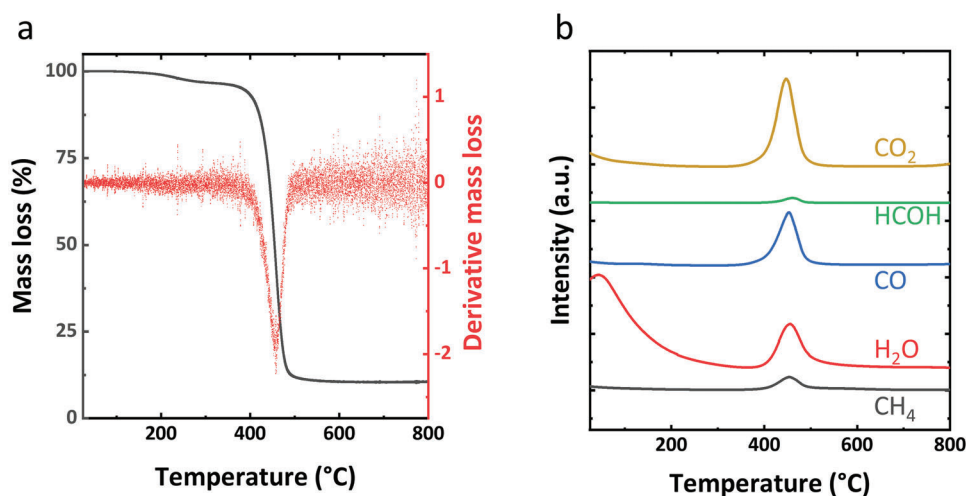


**Figure 2.** TGA of UV-cured IP-Dip polymer heated from room temperature to 820  $^{\circ}\text{C}$  with mass spectroscopy. a) Mass loss in % and its derivative during nonisothermal heating with 5  $^{\circ}\text{C s}^{-1}$  ramp rate in Ar atmosphere showing that the extremum of mass reduction happened at 458  $^{\circ}\text{C}$  with an onset of mass loss of 385  $^{\circ}\text{C}$ . b) Mass-spectrometric measurement of pyrolysis-induced volatile byproducts as a function of temperature indicating the formation of  $\text{CH}_4$ ,  $\text{H}_2\text{O}$ ,  $\text{CO}$ ,  $\text{HCOH}$ ,  $\text{CO}_2$ , etc.

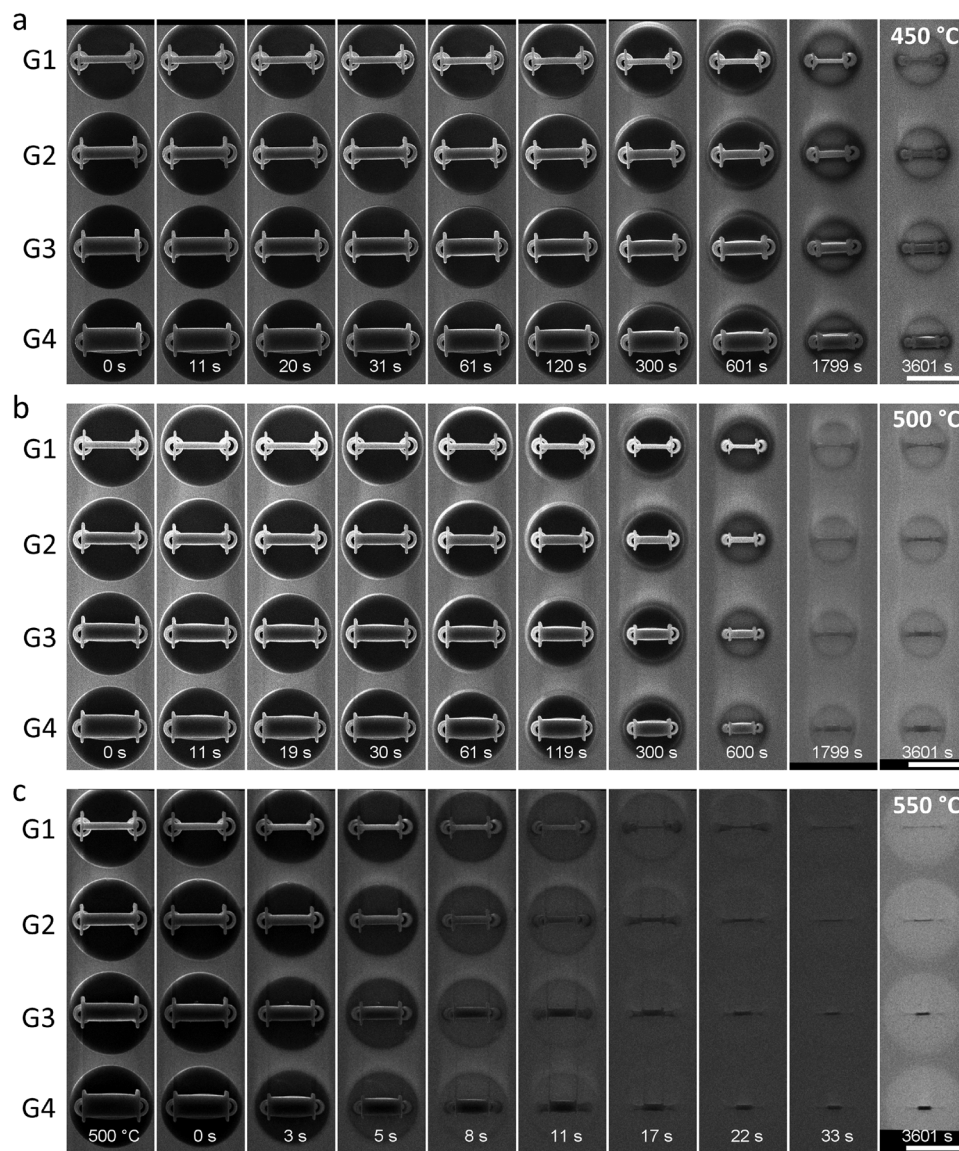


**Figure 3.** The evolution of 3D printed IP-Dip microstruts upon isothermal pyrolysis for one hour in a high vacuum. Montage of SEM images showing temporal sections of the pyrolysis-induced shrinkage process from a top view at a) 450, b) 500, and c) 550 °C, respectively. G1, G2, G3, and G4 represent microstruts with different as-printed cross-sectional dimensions, namely  $1 \times 1$ ,  $2 \times 2$ ,  $3 \times 3$ , and  $4 \times 4$   $\mu\text{m}$ , respectively. Timestamps indicating the pyrolysis duration are given in each subimage. The initial state of the microstruts at 500 °C is depicted in the first column of c), as it was observed that the first shrinkage caused by pyrolysis occurred at this temperature, before reaching the desired target temperature of 550 °C. Scale bars correspond to 10  $\mu\text{m}$ .

printed on the chips. To also study the effective surface area, the tetragonal microstruts differ in widths and heights, referred to as G1, G2, G3, and G4, corresponding to  $1 \times 1$ ,  $2 \times 2$ ,  $3 \times 3$ , and  $4 \times 4$   $\mu\text{m}$ , sharing the same as-printed length of 10  $\mu\text{m}$ .

At the beginning of isothermal heating, we observe the synchronous shrinkage of the disc pedestal and the microstruts over time while the microstruts remain upright without apparent deflection toward the substrate. As the degree of shrinkage progresses, the springs start to tilt, as apparent from the top view, while the pedestal shrinkage is restricted due to its adhesion to the substrate. By comparing the experiments at different temperatures in Figure 3a–c, it is evident that the higher the tem-

perature, the faster the shrinkage. Moreover, the final lengths at steady state conditions are smaller at higher temperatures. From a SEM perspective, imaging insulating materials, such as the polymer materials used here, without a metal coating is challenging due to the charging effect.<sup>[36]</sup> However, at higher temperatures, the transport of excess electrons is facilitated, making the direct imaging of the pyrolysis dynamics possible (See also Figure S4, Supporting Information). Nevertheless, the substrate still exhibits charging effect induced contrast inhomogeneities along the scan direction (e.g., scan direction from top to bottom in Figure 3) of the electron beam, especially in the regions between the disc pedestals where increased intensity is observed.

Moreover, apparent contrast differences between the microstruts themselves and the pedestals are due to differences in electron charge transport. While the pedestal is directly connected with its largest area to the substrate, which in turn is connected to the ground potential and therefore can better compensate electrically, the microstruts have only two points of contact with the substrate, namely via the spring feet. This slows down the electron transport and makes the microstruts appear brighter. In addition, the edge effect<sup>[36]</sup> makes the edges of the 3D-printed structures appear brighter than their insides because of the higher electron yield. Disregarding the local contrast variations explained above and considering the general contrast decrease from left to right, i.e., with increasing pyrolysis duration in Figure 3), this contrast change may give a direct indication of the pyrolysis-induced phase transformation from polymer to conductive carbon during in situ heating. For example, from the image series in Figure 3a, a polymer to conductive carbon transition is expected to take place after 1800 s at 450 °C, in Figure 3b after 600 s at 500 °C and in Figure 3c after 8 s at 550 °C. Although this contrast change is consistent with the expected tendency for this phase transformation to occur more rapidly at higher temperatures, we cannot ignore the fact that carbon contamination during continuous electron beam scanning can also change the overall contrast.<sup>[37]</sup> Similar observations were obtained for in situ pyrolysis in low vacuum (LV) conditions and the according image series are presented in Figure S3 (Supporting Information). The general observations for both atmospheres are: 1) the simultaneous shrinkage of the microstruts and the disk pedestal with increasing time; 2) the microstruts share a similar temperature dependence, namely the higher the temperature, the faster and higher the shrinkage. 3) Compared to HV, where the overall image contrast change indicates the phase transformation from polymer to conductive carbon, in LV this transition is not as pronounced. Only the in situ pyrolysis LV experiment at 550 °C indicates a transition within one hour, which however occurs at later times compared to HV. This implies a slower carbonization process in LV than that in HV, because the higher environmental pressure slows down the out-diffusion of volatile byproducts and in turn the polymer-to-carbon transition. More details are discussed in Section 2.5.

Tilting from the top view to a perspective view analysis, **Figure 4a**, one observes that not only the microstruts but also the springs and pedestals experienced structural deformation as well as bending. The original morphology of the springs has changed in that the windings are compressed and form a tubular structure. This is due to the softening of the material above its glass transition temperature ( $T_g$ ), which lies around 100 °C (see Figure S5, Supporting Information) combined with the shrinkage in the axial direction. The observed bending phenomenon in the microstruts can be explained by the semi-rubbery state above  $T_g$  and the mechanical stress caused by anisotropic shrinkage in the pedestal-spring-strut architecture. When the pedestal shrinkage is constrained early by the substrate contact, two forces induced by shrinkage act on the connection nodes of the microstruts and springs. This can be observed in the schematic force analysis of the G1 structure of the HV450 column in **Figure 4a**). There are two shrinkage-induced forces at the connection nodes of the microstruts and springs. The first is the force  $F_m$ , resulting from the shrinkage of the microstrut and directed toward

its center. The second is the force  $F_s$ , derived from spring shrinkage, which points along the spring toward the substrate. The resulting total force  $F_t$  is mainly directed downward toward the substrate, causing bending of the microstruts. In particular, the microstruts with the small cross sections, for example, G1 and G2 in **Figure 4a**, are more susceptible to this type of thermo-mechanical stress.<sup>[38]</sup> This bending phenomenon has not been previously observed in nanoarchitected metamaterials, which usually consist of multiple interconnected microstrut building blocks, suggesting an isotropic mechanical stress distribution.<sup>[6]</sup> As mentioned above, since the pedestal is directly connected to the substrate, its shrinkage at elevated temperatures is correspondingly limited. The degree of shrinkage of the pedestals is identical at 450 and 500 °C in HV condition, and degassing from above leads to sagging of the inner regions of the surface.<sup>[29]</sup> Notably, the pyrolyzed pedestals disappeared upon heating to 550 °C,<sup>[27]</sup> leaving a thin carbon residue layer on the substrate. At 550 °C of HV experiments, an elongation of the springs (due to the high deformation rate) resulted in different final dimensions of the individual microstruts: G1 (40%) and G2 (30%) show less shrinkage, while G3 and G4 are reaching the minimal sizes of 20%, which is similar to the shrinkage reported in other published works.<sup>[6,15]</sup>

In addition to the qualitative analysis, the projected length of the struts was tracked using the in situ videos to quantitatively describe the morphological evolution with respect to different temperatures, environments, and effective surfaces, shown in **Figure 4b–g**. **Figure 4b,d** depicts the kinetic relationship between the normalized length of the microstruts and the heating dwell time in HV environment. The different surface-to-volume ratios, G1–G4, show similar pyrolysis kinetics when exposed to heat under a high vacuum, including shrinkage rate and final length with extracted linear shrinkage of 45% (HV450) and 30% (HV500), respectively. Accordingly, **Figure 4e–g** represents the same results under LV conditions. The normalized length over time curves show an expected temperature dependency, namely the shrinkage rate is higher and the degree of shrinkage is increased with rising temperature. While the effective surface area of the microstruts (G1–G4) does not influence the shrinkage in HV environment, a noticeably effect of the surface-to-volume ratio is observed for the LV atmosphere, see **Figure 4e–g**. Higher surface-to-volume ratio ( $S_v$ ) of the microstruts lead to a higher shrinkage rate and degree. In addition, the overall observed rate and degree of shrinkage in the nitrogen atmosphere are lower than in high vacuum condition. For example, at 500 °C, G1–G4 under LV remain at 32%, 39%, 42%, and 45% of their initial lengths, respectively; in comparison, G1–G4 of HV experiments at the same temperatures have similar final lengths of 30%. The pyrolysis behavior change can be assigned to the varying diffusion process when desorbing volatile byproducts to the surrounding. Therefore, by controlling the arrangement of the building block dimensions in a microlattice, one may achieve unidirectional, multidirectional, or even more complex preferential shrinkage. Controlled pyrolysis with the help of atmospheric pressures requires a deep understanding of the interplay of shrinkage and intermediate mechanical properties. Additionally, it is important to consider that the length measured from above and at a right angle to the microstrut is actually a projection of the true length. This may result in a slight overestimation of the

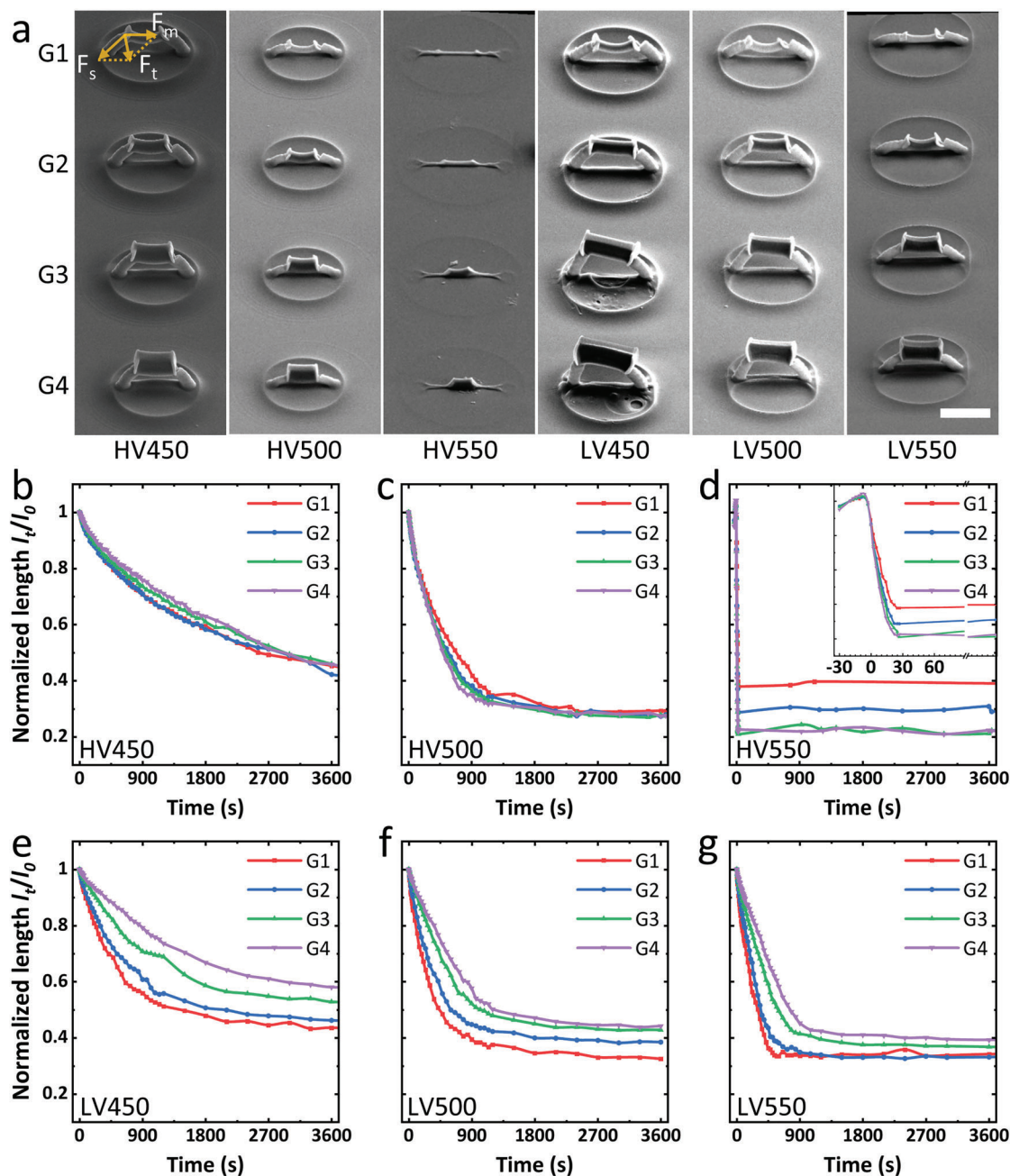


**Figure 4.** Comparison of microstrut shrinkage during isothermal pyrolysis in high vacuum (HV) and low vacuum (LV) conditions. Panel a) shows a postmortem analysis of the pyrolyzed microstruts at 450, 500, and 550 °C in both HV and LV environments, viewed from a 52° perspective angle. A schematic force analysis is depicted for the G1 structure of the HV450 column showing two shrinkage-induced forces at the connection nodes of the microstruts and springs. The force  $F_m$  is directed toward the center of the microstrut, while the force  $F_s$  derived from spring shrinkage points along its axis toward the substrate. The resulting total force  $F_t$  is mainly directed downward toward the substrate, causing the observed bending of the microstruts. Scale bars represent 5  $\mu\text{m}$ . b-d) Pyrolysis kinetics of high vacuum in situ heating experiments for the three temperatures: normalized length (projected) of each microstrut with respect to heating time in one hour. The inset in (d) showcases the initial stage of heating from room temperature up to 550 °C. The negative time range, which corresponds to the temperature ramp, reveals that the microstruts undergo thermal expansion until 500 °C, followed by structural shrinkage that saturates within about 30 s at 550 °C. e-g) Corresponding pyrolysis kinetics for the low vacuum in situ heating experiments.

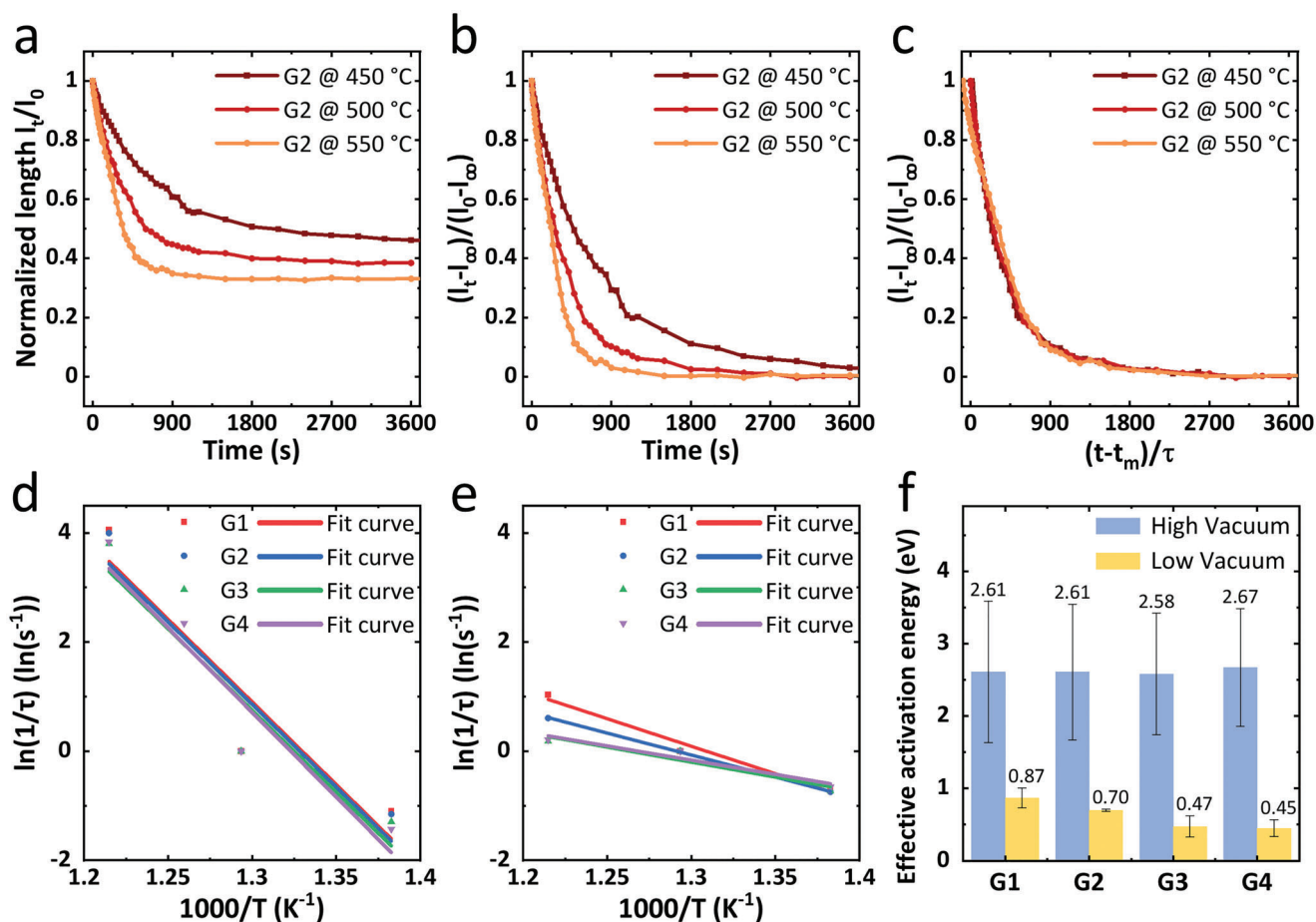


**Figure 5.** Effective activation energies derived from a model-free master curve approach. a–c) An example of master curve approach procedure by a curve rescaling to determine characteristic rates  $1/\tau$  of each heating temperature. a) Normalized length of microstrut G2 at different temperatures as a function of heating duration. b) Y-axis rescaling to conversion fraction. c) Time rescaling of the 450- and 550-°C curves onto the 500-°C curve, the master-curve. Arrhenius plottings of high d) and low e) vacuum pyrolysis to extract effective activation energies ( $E_a^{\text{eff}}$ ) of each microstrut from the slope of the fitted lines. f) Bar chart comparing the extracted  $E_a^{\text{eff}}$  for the microstruts with different cross-sections (G1–G4) in high and low vacuum conditions.

absolute length change and subsequent shrinkage. However, this does not affect the overall trend of the kinetic curves and will only marginally be influenced by the deviation in the slightly bent structures.

### 2.3. Master Curve Approach and Effective Activation Energy

In addition to the qualitative analysis of the pyrolysis-induced morphology kinetics, the effective activation energy ( $E_a^{\text{eff}}$ ) of different microstrut sizes can also be derived from the kinetic data. Therefore, we introduce the model-free master curve method to derive the  $E_a^{\text{eff}}$ .<sup>[23]</sup> A commonality is clearly seen from the kinetic curves of HV and LV: the curves fall at different speeds to different constant values for the different temperatures. The prerequisite for the master curve method is the similarity of the kinetic curves, that is, the time-temperature equivalence of the pyrolysis process. Note that quantitative statistical results can only be accepted if the beam damage is negligible. A comparison of electron beam irradiated and non-irradiated heated samples concluded a cutoff

temperature for electron beam damage at around 450 °C at the given electron beam parameter, see Figure S6 (Supporting Information).

The basic idea of how the master curve approach is applied to extract the  $E_a^{\text{eff}}$  is illustrated in Figure 5a–c. The Arrhenius law, used to determine the relationship between the rate of a chemical reaction  $k$  and temperature  $T$  in Kelvin, is expressed as:

$$k = A e^{-E_a/k_B T} \quad (1)$$

where  $A$ ,  $E_a$ , and  $k_B$  are pre-exponential factor, activation energy, and Boltzmann constant, respectively. We rescaled the curves  $l(t)$  of a single microstrut (G2) with the expression:

$$\left(\frac{t - t_m}{\tau}\right) \rightarrow \left(\frac{l - l_\infty}{l_0 - l_\infty}\right) \quad (2)$$

to obtain the characteristic rate at different temperatures. First, we extracted three different temperature curves from LV in situ experiments as shown in Figure 5a. By rescaling the y-axis, the

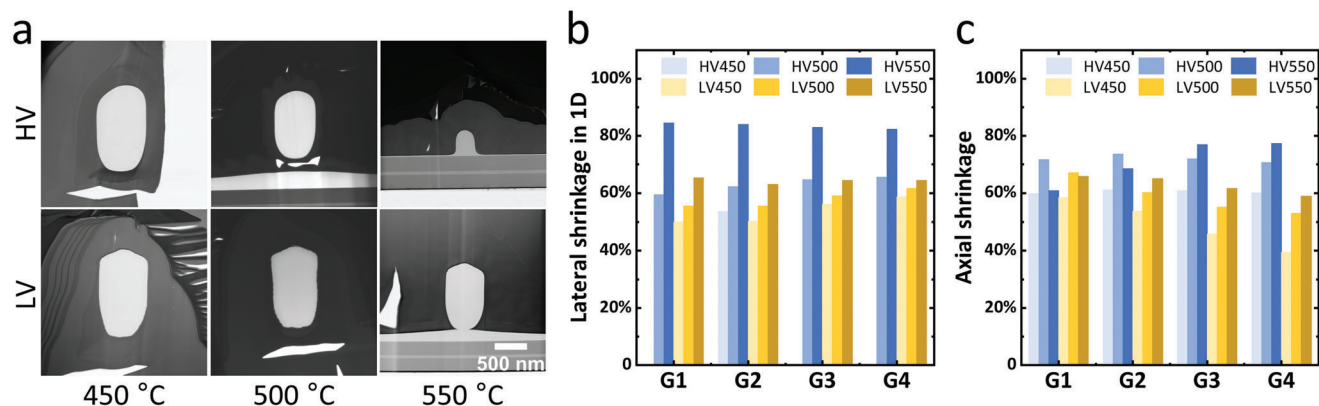


**Figure 6.** Cross-sectional characterization of the pyrolyzed microstruts. a) Bright-field STEM images of cross-sections of G2 microstruts after exposure to various pyrolysis conditions (e.g., temperature and environment). Comparison of the degree of linear shrinkage in cross-sectional (lateral) b) and axial c) direction between high and low vacuum pyrolysis with respect to the different microstruts.

normalized length  $l$  is converted into the conversion degree  $\left(\frac{l-l_\infty}{l_0-l_\infty}\right)$  of the actual time  $t$ , starting from 1 and ending at 0, as shown in Figure 5b. Here  $l$ ,  $l_0$ , and  $l_\infty$  represent the normalized length of the actual time  $t$ , the initial and final lengths, respectively. In this way, the three temperature curves of G2 share the same span. For the x-axis rescaling, one of the heating experiments is chosen as a reference, i.e., the master curve. The other curves are rescaled to overlap with the master curve by adjusting the characteristic time  $\tau$  and offset  $t_m$  by least squares fitting. In our case, the curve with the intermediate temperature of 500 °C is selected as the master curve for the best curve overlap (Figure 5c). The pyrolysis kinetic information is then extracted as the characteristic time  $\tau$  and its characteristic rate  $\tau^{-1}$ . Finally, Arrhenius plotting of the characteristic rates and subsequent linear fitting in Figure 5d,e are performed to retrieve the slope and  $E_a^{eff}$  of G1–G4 in different environments as shown in Figure 5f. All calculation procedures and details are shown in the Supporting Information.

The results indicate a  $S_V$ -independent activation energy in HV with a value around 2.6 eV and  $S_V$ -dependent activation energies in LV, ranging from 0.5 – 0.9 eV. It is remarkable that the value of  $E_a^{eff}$  changes significantly with the varying pressure by a factor of four. This points out a change in the overall mechanism of pyrolysis, which can be addressed by the kinetic model of typical polymer pyrolysis. In this model the chemical reactions are happening on the materials' surface and is referred to the so called geometric shrinkage model.<sup>[39]</sup> During the structural evolution, several reactions occur in parallel or succession, such as the pyrolysis-induced formation of volatile byproducts and a series of physical molecular transports: from the microstrut core to its surface, from the solid interface to the surrounding environment, leading to the complexity of the pyrolysis reaction. An important factor is the residence time of volatile byproducts in the solid, including water vapor, carbon monoxide, carbon dioxide, and various hydrocarbons (determined by TGA-MS analysis in Figure 2b), which are influenced by the surrounding atmosphere. The mobile gas molecules can undergo exothermic secondary reactions with their surroundings or effectively transfer heat to their neighboring molecules, resulting in the decomposition of polymer precursors and the formation of carbon.<sup>[40]</sup> An in-

creased atmospheric pressure slows down the gas diffusion processes and facilitates more second-order reactions, which can be associated with the different extracted  $E_a^{eff}$  in low vacuum experiments. This can also explain why thicker samples have smaller activation energies and more carbon residues due to a longer gas residence time. However, to evaluate morphological evolution precisely, one has to consider the interface and surface energy of each component (polymer, volatile gas, and carbon).<sup>[41]</sup>

#### 2.4. Cross-Sectional TEM Study of the Pyrolyzed Microstruts

To get more insights into the influence of surface-to-volume ratio ( $S_V$ ), temperature, and environmental pressure on the pyrolysis-induced morphology evolution, we investigate the microstructure and elemental distribution from cross-sections of the heated samples. Lamellae of pyrolyzed microstrut samples for TEM studies were prepared by a focussed ion beam (FIB)-lift-out technique. **Figure 6a** reveals bright field-STEM micrographs of the cross-sections of the pyrolyzed G2 microstruts (originally having as-printed lateral dimensions of 2x2  $\mu\text{m}$ ) for the different heating and environmental pyrolysis conditions. We refer to the different environment and temperature conditions as HV450, HV500, HV550, and LV450, LV500, LV550. The cross-sections of the microstruts appear bright in the center of the images and due to sample preparation reasons are embedded in platinum-carbon deposits. As mentioned above, the elongation in z-direction is due to the printing resolution limitation in the vertical direction of TPL.

We observe a special behavior for the HV550 sample series, where the heated microstruts ended up coming into contact with the substrate due to the failure of synchronous contraction of the support structures. Rapid heating up to 550 °C might lead to the disappearance of the pedestal and the rapid collapse of the spring. The merging of the strut and pedestal indicates that the polymer undergoes a rubbery state during the pyrolysis process. Besides, this semi-solid intermediate material is also responsible for the final smooth and spheroidized surfaces to minimize the surface energies.<sup>[42]</sup> This rubbery material state induces a flow on the substrate, yielding a wider base, see Figure 6a HV

550 °C. When comparing samples with different thicknesses under the same heating conditions (See Figure S10, Supporting Information), we found that the thinner samples showed more elliptical and smoother surfaces. The lower curvature of the downward facing positions closer to the substrate can be attributed to downward bending. Another notable phenomenon is a rough contour on the surfaces of G3 and G4 heated under LV450 and LV500 conditions. This may be caused by the retention and bursting of volatile gases during rapid heating under atmospheric pressure. This phenomenon was also reported on the surface of macroscale samples pyrolyzed with a high heat ramp of 50 °C min<sup>-1</sup>.<sup>[22]</sup>

Image segmentation was utilized to accurately extract the cross-sectional area of the distorted and as-printed microstruts. The lateral shrinkage under various geometries and heating conditions was determined (as shown in Figure 6b by calculating the equivalent length of the square's side using the square root of the cross-sectional area, assuming a semi-square design to account for the distorted cross-sectional shapes). It can be concluded that the shrinkage in lateral direction under HV conditions is higher than that of LV conditions, which is consistent with the tendency in the axially directed shrinkage. By comparing the degrees of shrinkage in lateral and axial directions (Figure 6c), we find interesting phenomena. In HV, the shrinkage in the lateral direction, which is  $S_V$ -independent, is smaller than that of the axial direction, minimizing the surface energy. However, in LV condition, there is a reversed relationship between  $S_V$  and the lateral shrinkage, *i.e.*, thick struts have a higher degree of cross-sectional shrinkage compared to that of thin struts. This results in a competition between shrinkage degrees in lateral and axial directions with respect to the aspect ratio. Moreover, the LV surface-to-volume ratio effect is less pronounced in the cross-sectional shrinkage than on axial, which may be explained by the inhomogeneous cross-sectional sizes due to bending and an inaccurate estimate of the initial cross-sectional area. However, the axial shrinkage determines the shrinkage of the nano architected lattice structures composed of multiple microstruts. Attention should be assigned to the possible anisotropy of pyrolytic shrinkage in an inert atmosphere when using struts of different thicknesses. Here, we suggest performing high vacuum pyrolysis for precise structural control by excluding the influence of gas desorption reactions based on an altered chemical potential in low vacuum conditions.

We analyzed the chemical fingerprint and elemental distribution of cross-sectional samples by STEM-EELS spectrum imaging. Figure 7a shows the core-loss EELS (C-K edge with O-K edge as insert) of the residual carbon derived from the IP-Dip microstruts after pyrolysis at 550 °C from HV and LV, respectively. All spectra from high and low vacuum heating at 450 °C and 550 °C share similar amorphous features: ionization of the K-shell electrons with transitions into  $\pi^*$  orbitals (C=C,  $sp^2$ ) at 284 eV and a transition to  $\sigma^*$  orbitals (C-C,  $sp^3$  hybrid) as broad contribution starting at around 290 eV. In contrast, glassy carbon or graphenoid materials would feature a sharp first loss peak at 284 eV and an increased  $sp^2/sp^3$  ratio larger than one, which are not observed in the in situ heated microstruts in the temperature range of 450 to 550 °C. The EELS results are consistent with the literature, that pyrolytic carbon from IP-Dip below 700 °C is predominantly amorphous.<sup>[43]</sup>

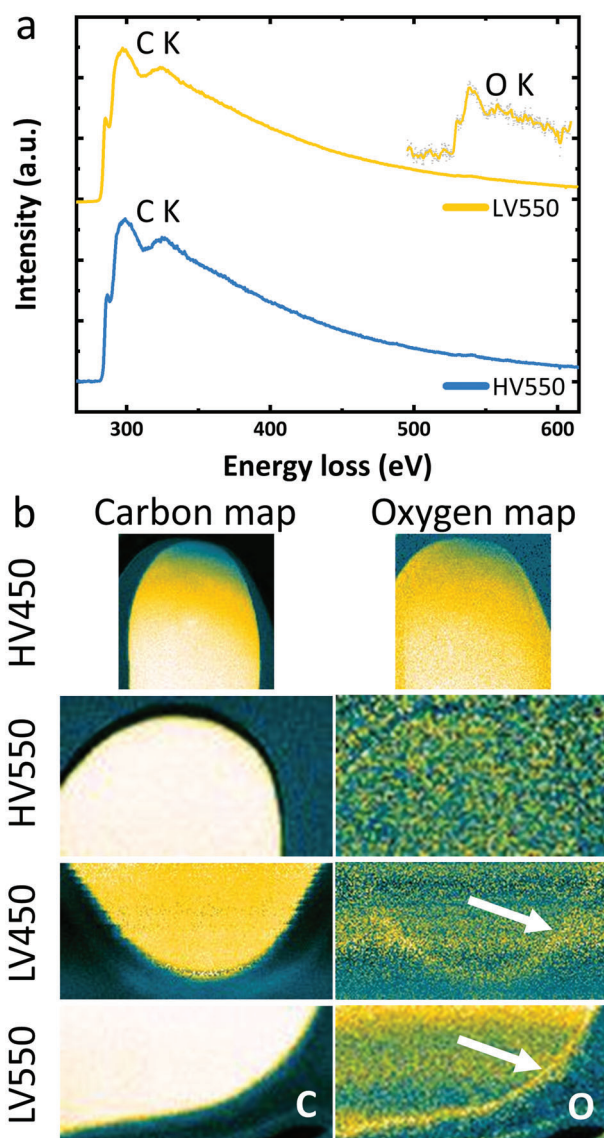


**Figure 7.** Local chemical analysis of pyrolyzed microstruts under different heating conditions by STEM-EELS. a) Core-loss EELS spectra of HV550 and LV 550 samples containing carbon and oxygen K-shell ionization edges. b) Two columns of spectrum images showing the carbon (left) and oxygen (right) distribution in the microrstruts cross-sections. Interestingly an oxygen accumulation close to the surface of the samples under low vacuum conditions is observed.

Figure 7b shows spectral images of carbon and oxygen (the main elemental constituents of IP-Dip) from different pyrolysis conditions. To obtain the elemental mappings, inelastically scattered electrons are collected with a spatial resolution of 2–6 nm over the range of ionization energies for the K shells of the desired elements. The results show a uniform carbon distribution in all heated samples, except the HV450 case, due to the low intensity of the thickness-dependent EELS signal at the thin edge. Surprisingly, we observed a different distribution of the oxygen signal. In spite of the noisy footprint of oxygen due to the limited acquisition time, we found an accumulation of oxygen at the edges of the low-vacuum heated samples, which was not

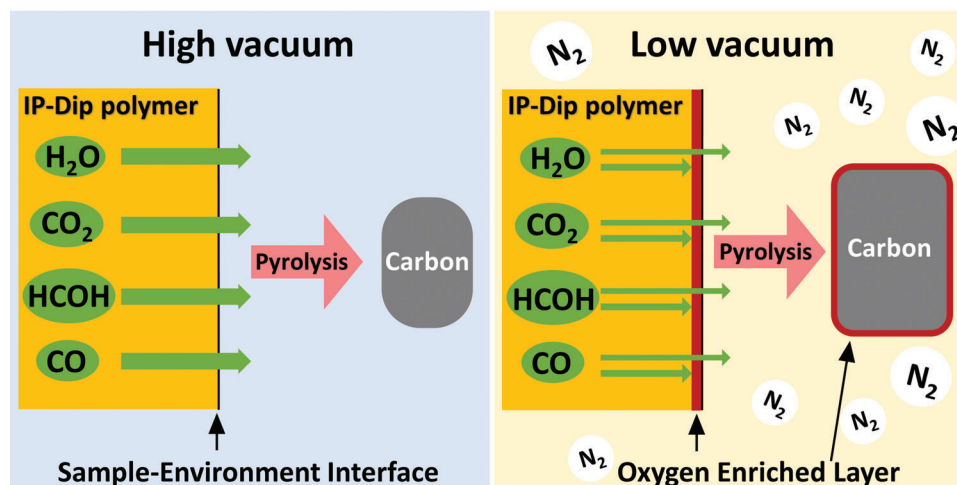


**Figure 8.** Schematic of IP-Dip polymer precursor pyrolysis mechanism in high vacuum and low vacuum conditions. An increased partial pressure hinders gas desorption and thus promotes second-order reactions, which result in more carbon yield and an oxygen ring at the sample surface.

observed in high-vacuum samples. This result indicates that the oxygen-containing volatile byproducts, mainly carbon monoxide and carbon dioxide, were indeed released slowly in the material, and desorption of these volatile components is hindered by the increased pressure in the surrounding environment.

## 2.5. Morphological Mechanism During Pyrolysis

We systematically evaluated the morphological evolution and chemical footprints of IP-Dip-derived microstruts under various heating temperatures in high and low vacuum modes. The discussion leads to a morphological mechanism from several aspects. The inherent volumetric reduction during pyrolysis of the polymer precursor is predominantly caused by degassing,<sup>[29,38]</sup> followed by the desorption of the generated volatile gases. It has to be noted that the degassing process is affected by the conversion rate of cured polymer into volatile byproducts, as well as physical diffusion from the interior of the structures toward the surfaces and the subsequent desorption. The former is mainly controlled by heating temperature, while the latter is an interplay between several parameters, such as the environmental pressure and an effective surface area.

Heating a polymeric structures above its degradation temperature leads to volatilization of the formed gaseous components and results in a carbon reconfiguration that can create a non-graphitic carbon, namely pyrolytic carbon (PyC).<sup>[20,42]</sup> Increasing temperature is hereby responsible for different pyrolysis stages that can be summarized as degassing, radical activation, C-C bond formation, and further graphitization. Our work focuses on the initial temperature stage from 450 to 550 °C, where significant mass loss and, therefore, structural shrinkage occurs. Upon increasing the heating temperatures, a dramatic acceleration of size reduction was observed for both vacuum modes (HV and LV), which resulted from the boosted degassing rate. Nevertheless, it is believed that pyrolysis at moderate temperatures leads to the formation of dangling bonds, which in turn can rearrange and anchor together, leading to less mass loss, ending shrinkage

and achieving a steady state.<sup>[34]</sup> The evolution of graphene-like fragments, formed in pyrolyzed carbon microstructures, upon heating above 1000 °C is extensively studied by in situ TEM.<sup>[21,44]</sup> Moreover, molecular dynamic simulations confirm that phenol rings and non-six-membered rings form at elevated temperatures, as studied for the pyrolysis of 16 monomeric precursors in [45].

The environmental pressure for the pyrolysis process plays an important role in degassing, as it directly influences physical diffusion<sup>[29]</sup> and possible subsequent exothermic reactions, as shown in **Figure 8**. High vacuum pyrolysis yields a faster and higher shrinkage than heating in a nitrogen atmosphere with increased partial pressure by five orders of magnitude. This implies a rapid desorption process from the interface between the sample and the surrounding environment in a low-pressure condition (HV). In contrast, for LV, the slowed diffusion and desorption or, in other words, the extended residence time of the volatile byproducts within the 3D-printed structures entails a higher probability of second-order reactions, leading to two further consequences: 1) a higher yield of pyrolytic carbon occurs and 2) the formation of an oxygen-enriched surface shell is promoted. The additional energy source of the system, such as second-order exothermic reactions<sup>[40]</sup> and the heat transfer from the gas to the sample<sup>[46]</sup> is consequently reflected in the reduction of the effective activation energies in low vacuum mode.

We have investigated how the surface-area-to-volume ratio ( $S_V$ ) affects structural degradation during pyrolysis. It is generally believed that a higher  $S_V$  can lead to faster shrinkage due to faster degassing,<sup>[29,38]</sup> which is in line with our experiments in low vacuum. However, we found that when a high vacuum atmosphere is used, the different  $S_V$  instead experience identical shrinkage, hence the  $S_V$  effect on shrinkage behavior is missing in HV. These findings can be used to prevent thermally induced undesired deformation in complex structures.

The use of TPL in conceiving structures for pyrolytic experiments has boosted the complexity of geometry,<sup>[1]</sup> while the material choice is limited to cross-linkable polymers,<sup>[47]</sup> such as the acrylate-based IP-series and the epoxy-based SU-8

photoresist, which are widely used in pyrolytic carbon fabrication. A lower carbon yield and a more pronounced size reduction of IP-Dip-based structures, in comparison to structures made from SU-8, have been ascribed to a larger fraction of bonded oxygen in IP-Dip.<sup>[27]</sup> Last but not least, a simulation work in literature examined the significant effect of the interface energy and surface energies of each component (polymer, carbon, volatile byproduct) on the morphological evolution during pyrolysis.<sup>[41]</sup> Thus, further work can include not only the experimental studies of the effect of different pyrolysis parameters on morphological evolution and material properties but also simulation work on the influence of surface and interface energies on the final structure.

### 3. Conclusion

In summary, the morphological dynamics of 3D microstruts with different surface-to-volume ratios during isothermal heating under two environmental conditions, high vacuum and nitrogen atmosphere with low vacuum, were investigated by in situ ESEM heating of supported microstruts, fabricated by TPL from IP-Dip. By evaluation of the pyrolysis-induced size reduction, a faster and higher shrinkage was observed with increasing temperatures from 450, 500, to 550 °C, decreasing partial pressure from three to around  $10^{-5}$  mbar and higher surface-to-volume ratio. In our proposed degassing-based morphological mechanism, the structural shrinkage and deformation are tunable by a chemical reaction rate coupled to a physical diffusion process, which is linked to several processing parameters, including heating temperature, environmental pressure, surface-to-volume ratio, and degree of cross-linking. A model-free master curve approach was used to calculate the effective activation energy of high vacuum pyrolysis with 2.6 eV and nitrogen atmosphere heating with 0.5–0.9 eV from axial shrinkage kinetics data. Furthermore, an oxygen accumulation on the edge of low-vacuum pyrolyzed sample was revealed by the postmortem STEM-EELS analysis of the microstruts' cross-sections, which strengthens the hypothesis of second-order reactions for the desorption of volatile gases, containing CO and CO<sub>2</sub>, resulting in a lower effective activation energy in low vacuum heating. The missing surface-to-volume ratio effect in high vacuum experiments demonstrated a parameter competition on pyrolysis behaviors, which can be utilized to develop isotropic shrinkage of complex structures. While in the atmospheric environment, controlled pyrolysis of structures with different geometrical dimensions will allow to specifically tailor shrinkage during pyrolysis and create tensegrity structures. Our study offers a way for the fundamental understanding of the morphological evolution under different pyrolysis conditions and can be employed to design and fabricate precise carbon structures feeding the need for miniaturized C-MEMS and NEMS.

### 4. Experimental Section

**Fabrication:** 3D microstruts were fabricated on the SiN<sub>x</sub> membrane of heating nano-chips (Lightning 4h2b type, DENSsolutions) using 3D-DLW (Photonic Professional GT2, Nanoscribe) Dip-in laser lithography configuration. The commercial photoresist IP-Dip (Nanoscribe) was chosen as a case-study precursor due to its high resolution and successfully pyrolyzed structure.<sup>[6]</sup> DLW was conducted using a 63x objective lens (Nanoscribe)

for fine structure printing. The printing parameters utilized were as follows: microstruts were printed layer-by-layer with a constant distance of 200 nm between two adjacent voxel lines in all three dimensions. A constant laser power of 40% (approximately 10.6 mW) and a constant scan speed of 3000 μm s<sup>-1</sup> were used.

A series of tetragonal microstruts were designed with dimensions of 10 × 1 × 1 μm to 10 × 4 × 4 μm to study surface-to-volume ratio dependence upon pyrolysis. These microstruts were anchored on a cylindrical pedestal base with a height of 3 μm for an isotropic structural shrinkage during heating. They were supported by two coil springs with six windings and a size of 10 μm to support them on the surface elastically. This design helped obtain a pure material response to the thermal stimuli within a specific contraction range. The printing codes of microstruts were published via zenodo platform with DOI 10.5281/zenodo.7405219.

After printing, the sample was developed by PGMEA for 20 min and subsequently by isopropanol for 5 min to wash away the unpolymerized photoresist. The final drying procedure was carried out by a critical point dryer (Leica EM CPD300) to maintain the structure.<sup>[48]</sup>

**In Situ Pyrolysis in ESEM:** In situ heating experiments were performed on the DENSsolution TKD holder and Lightning chip. It used a high ramping rate of 20 °C s<sup>-1</sup> to reach temperature set points (450, 500, and 550 °C) rapidly (nonisothermal heating) by climate software (Denssolutions). The structural evolution was monitored in a top-view geometry by continuous secondary electron image acquisition.

Two vacuum conditions were used to perform in situ heating experiments: high vacuum ( $10^{-5}$  to  $10^{-6}$  mbar) and low vacuum of 3 mbar with nitrogen gas in ESEM mode. In high vacuum mode, ETD was used as a secondary electron detector. It switched to GSED with a smaller aperture size in low vacuum mode.

To purify the inert atmosphere, the low vacuum experiment was first set to high vacuum to pump out air molecules. To discuss electron beam damage on polymer samples, two identical structures were printed on the same heating chip, one for electron irradiation and another one was kept outside movie frame (beam nonirradiated). Both were characterized after heating and compared in supporting information.

**Post TEM Characterization:** Heated samples were characterized at FIB-SEM (FEI Strata 400S) instead of an SEM with a large tilting angle of 52° for side view. After pyrolysis, samples were sputtered with 5 nm Pt for sufficient electrical conductance and minimized electron charging effect during measurement by Leica ACE600 coater.

In a cross-sectional TEM study, thin TEM specimens were prepared from heated microstruts by the FIB lift-out technique (FEI Strata 400S dual-beam system and Thermo Fisher Helios G4 FX NanoLab). To protect the structure and fill the gap between the SiN<sub>x</sub> substrate and heated struts, Pt electron beam deposition and FIB deposition were performed with a height of around 5–7 μm. Thin TEM cross-sections were characterized by BF and DF STEM imaging with a FEI Titan<sup>3</sup> 80–300 operated at 300 kV. Chemical analysis of carbon and oxygen elements was carried out by STEM-EELS technique with a post-column Gatan Imaging Filter (GIF) (Tridiem 865 ER) and a Gatan CCD camera (Ultrascan 1000).

**Thermogravimetry-Mass Spectrometry (TG-MS):** TG-MS analysis was performed by SENSYS evo TG-DSC (Setaram) equipped with Pfeiffer Omnistar GSD 320 mass spectrometer.

### Supporting Information

Supporting Information is available from the Wiley Online Library or from the author.

### Acknowledgements

All authors appreciate the financial support by the German Research Foundation (Deutsche Forschungsgemeinschaft, DFG) under Germany's Excellence Strategy via the Excellence Cluster 3D Matter Made to Order (EXC-2082/1-390761711). The authors thank Stefan Hengsbach of KNMFi for his assistance in printing the microstruts. All the authors thank Karlsruhe Institute of Technology for the support to continue research in a safe

and healthy environment during the adverse period of the COVID-19 pandemic.

Open access funding enabled and organized by Projekt DEAL.

## Conflict of Interest

The authors declare no conflict of interest.

## Data Availability Statement

The data that support the findings of this study are available from the corresponding author upon reasonable request.

## Keywords

3D printing, in situ electron microscopy, metamaterials, pyrolysis, two-photon lithography

Received: February 28, 2023

Revised: May 9, 2023

Published online:

- [1] J. Bauer, L. R. Meza, T. A. Schaedler, R. Schwaiger, X. Zheng, L. Valdevit, *Adv. Mater.* **2017**, *29*, 1701850.
- [2] K. Malladi, C. Wang, M. Madou, *Carbon* **2006**, *44*, 2602.
- [3] C. Wang, G. Jia, L. H. Taherabadi, M. J. Madou, *J. Microelectromech. Syst.* **2005**, *14*, 348.
- [4] J. Z. Manapat, Q. Chen, P. Ye, R. C. Advincula, *Macromol. Mater. Eng.* **2017**, *302*, 1600553.
- [5] C. Sun, N. Fang, D. M. Wu, X. Zhang, *Sensors and Actuators A: Physical* **2005**, *121*, 113.
- [6] J. Bauer, A. Schroer, R. Schwaiger, O. Kraft, *Nat. Mater.* **2016**, *15*, 438.
- [7] G. Seniutinas, A. Weber, C. Padeste, I. Sakellari, M. Farsari, C. David, *Microelectron. Eng.* **2018**, *191*, 25.
- [8] C. Yang, Q. Cao, P. Puthongkham, S. T. Lee, M. Ganesana, N. V. Lavrik, B. J. Venton, *Angew. Chem., Int. Ed.* **2018**, *57*, 14255.
- [9] G. Mernier, R. Martinez-Duarte, R. Lehal, F. Radtke, P. Renaud, *Micromachines* **2012**, *3*, 574.
- [10] J. J. V. Dersarl, A. Mercanzini, P. Renaud, *Adv. Funct. Mater.* **2015**, *25*, 78.
- [11] F. Pérennès, B. Marmiroli, M. Matteucci, M. Tormen, L. Vaccari, E. D. Fabrizio, *J. Microelectromech. Syst.* **2006**, *16*, 473.
- [12] R. Mishra, B. Pramanick, T. K. Maiti, T. K. Bhattacharyya, *Microsyst. Nanoeng.* **2018**, *4*, 38.
- [13] M. Islam, A. D. Lantada, D. Mager, J. G. Korvink, M. Islam, D. Mager, J. G. Korvink, A. D. Lantada, *Adv. Healthcare Mater.* **2022**, *11*, 2101834.
- [14] L. Amato, A. Heiskanen, C. Caviglia, F. Shah, K. Zór, M. Skolimowski, M. Madou, L. Gammelgaard, R. Hansen, E. G. Seiz, M. Ramos, T. R. Moreno, A. Martínez-Serrano, S. S. Keller, J. Ernés, *Adv. Funct. Mater.* **2014**, *24*, 7042.
- [15] Y. Liu, H. Wang, J. Ho, R. C. Ng, R. J. Ng, V. H. Hall-Chen, E. H. Koay, Z. Dong, H. Liu, C. W. Qiu, J. R. Greer, J. K. Yang, *Nat. Commun.* **2019**, *10*, 4340.
- [16] J. Kim, X. Song, K. Kinoshita, M. Madou, R. White, *J. Electrochem. Soc.* **1998**, *145*, 2314.
- [17] R. L. McCreery, *Chem. Rev.* **2008**, *108*, 2646.
- [18] J. C. Lewis, B. Redfern, F. C. Cowlard, *Solid-State Electron.* **1963**, *6*, 251.
- [19] S. Sharma, M. Madou, *Bioinspired, Biomimetic and Nanobiomater.* **2012**, *1*, 252.
- [20] G. Jenkins, K. Kawamura, *Polymeric carbons: carbon fibre, glass and char*, Cambridge University Press, Cambridge, UK; New York, USA, **1976**.
- [21] S. Sharma, C. N. S. Kumar, J. G. Korvink, C. Kübel, *Sci. Rep.* **2018**, *8*, 16282.
- [22] S. Sharma, R. Kamath, M. Madou, *J. Anal. Appl. Pyrolysis* **2014**, *108*, 12.
- [23] F. Niekpiel, P. Schweizer, S. M. Kraschewski, B. Butz, E. Spiecker, *Acta Mater.* **2015**, *90*, 118.
- [24] X. Zhang, L. Zhong, A. Mateos, A. Kudo, A. Vyatskikh, H. Gao, J. R. Greer, X. Li, *Nat. Nanotechnol.* **2019**, *14*, 762.
- [25] C. M. Portela, B. W. Edwards, D. Veyssset, Y. Sun, K. A. Nelson, D. M. Kochmann, J. R. Greer, *Nat. Mater.* **2021**, *20*, 1491.
- [26] J. Bauer, J. A. Kraus, C. Crook, J. J. Rimoli, L. Valdevit, J. Bauer, L. Valdevit, J. A. Kraus, J. J. Rimoli, C. Crook, *Adv. Mater.* **2021**, *33*, 2005647.
- [27] A. Zakhurdaeva, P. I. Dietrich, H. Hölscher, C. Koos, J. G. Korvink, S. Sharma, *Micromachines* **2017**, *8*, 285.
- [28] C. Gunderson, N. Rohbeck, M. Tranchant, J. Michler, L. Philippe, C. Gunderson, N. Rohbeck, M. Tranchant, J. Michler, L. Philippe, *Adv. Eng. Mater.* **2021**, *23*, 2001293.
- [29] R. Natu, M. Islam, J. Gilmore, R. Martinez-Duarte, *J. Anal. Appl. Pyrolysis* **2018**, *131*, 17.
- [30] M. I. Sharipova, T. G. Baluyan, K. A. Abrashitova, G. E. Kulagin, A. K. Petrov, A. S. Chizhov, A. S. Chizhov, T. B. Shatalova, D. Chubich, D. A. Kolyagin, A. G. Vitukhnovsky, A. G. Vitukhnovsky, V. O. Bessonov, V. O. Bessonov, A. A. Fedyanin, *Opt. Mater. Express* **2021**, *11*, 371.
- [31] C. M. Kurpiers, S. Hengsbach, R. Schwaiger, *MRS Adv.* **2021**, *6*, 507.
- [32] L. Molina-Luna, S. Wang, Y. Pivak, A. Zintler, H. H. Pérez-Garza, R. G. Spruit, Q. Xu, M. Yi, B. X. Xu, M. Acosta, *Nat. Commun.* **2018**, *9*, 4445.
- [33] H. H. P. Garza, Y. Pivak, L. M. Luna, J. T. van Omme, R. G. Spruit, M. Sholkina, M. Pen, Q. Xu, in *2017 19th International Conference on Solid-State Sensors, Actuators and Microsystems (TRANSDUCERS)*, IEEE, New York **2017**, pp. 2155–2158.
- [34] B. Rezaei, J. Y. Pan, C. Gundlach, S. S. Keller, *Mater. Des.* **2020**, *193*, 108834.
- [35] B. Pramanick, M. Vazquez-Pinon, A. Torres-Castro, S. O. Martinez-Chapaa, M. Madou, *Mater. Today: Proc.* **2018**, *5*, 9669.
- [36] L. Reimer, *Image Contrast and Signal Processing*, Springer Berlin Heidelberg, Berlin, Heidelberg **1998**, pp. 207–251.
- [37] M. Hugenschmidt, K. Adrion, A. Marx, E. Müller, D. Gerthsen, *Microw. Microanal.* **2022**, *22*, 219.
- [38] B. Cardenas-Benitez, C. Eschenbaum, D. Mager, J. G. Korvink, M. J. Madou, U. Lemmer, I. D. Leon, S. O. Martinez-Chapa, *Microsyst. Nanoeng.* **2019**, *5*, 38.
- [39] Y. Zhang, Z. Fu, W. Wang, G. Ji, M. Zhao, A. Li, *ACS Sustainable Chem. Eng.* **2022**, *10*, 91.
- [40] J. M. Encinar, J. F. González, *Fuel Process. Technol.* **2008**, *89*, 678.
- [41] M. Yang, W. Lee, H. Shin, D. Kim, *J. Nanomater.* **2015**, *2015*, 931429.
- [42] S. Sharma, *Materials* **2018**, *11*, 1857.
- [43] J. B. Tyler, G. L. Smith, A. C. Leff, P. M. Wilson, J. Cumings, N. Lazarus, *Adv. Eng. Mater.* **2021**, *23*, 2001027.
- [44] C. N. S. Kumar, M. Konrad, V. S. K. Chakravadhanula, S. Dehm, D. Wang, W. Wenzel, R. Krupke, C. Kübel, *Nanoscale Adv.* **2019**, *1*, 2485.
- [45] R. Montgomery-Walsh, S. Nimbalkar, J. Bunnell, S. L. Galindo, S. Kassegne, *Carbon* **2021**, *184*, 627.
- [46] J. Su, A. C. Lua, *J. Membr. Sci.* **2007**, *305*, 263.
- [47] C. Barner-Kowollik, M. Bastmeyer, E. Blasco, G. Delaittre, P. Müller, B. Richter, M. Wegener, *Angew. Chem., Int. Ed.* **2017**, *56*, 15828.
- [48] S. Maruo, T. Hasegawa, N. Yoshimura, *Opt. Express* **2009**, *17*, 20945.